Published in final edited form as:
Nano Lett. 2009 July ; 9(7): 2676–2682. doi:10.1021/nl901129j.

Parallax: High Accuracy Three-Dimensional Single Molecule Tracking Using Split Images

Yujie Sun[1,2], **Jennine Dawicki McKenna**[1,3], **John M. Murray**[4], **E. Michael Ostap**[1,3], and **Yale E. Goldman**[1,2,3,*]

[1] Pennsylvania Muscle Institute, University of Pennsylvania, 3700 Hamilton Walk, Philadelphia, PA 19104

[2] Nano/Bio Interface Center, University of Pennsylvania, 3700 Hamilton Walk, Philadelphia, PA 19104

[3] Department of Physiology, University of Pennsylvania, 3700 Hamilton Walk, Philadelphia, PA 19104

[4] Department of Cell and Developmental Biology, University of Pennsylvania, 3700 Hamilton Walk, Philadelphia, PA 19104

Abstract

Three-dimensional (3D) tracking can provide valuable biological insights that are missing in conventional microscopy. Here we developed a single molecule 3D tracking microscopy technique, named *Parallax*, with high localization precision and temporal resolution. We demonstrated its capabilities by studying the 3D trafficking of glucose-transporter-4 containing vesicles in living adipocytes as well as the walking path of single myosin VI molecules along actin filaments.

Many biological investigations require 3D tracking of small objects, such as vesicles and single molecules with microscopic resolution. A number of groups have developed techniques for 3D tracking by optical microscopy based on confocal imaging,[1–3] multiple *z*-slice imaging,[4–7] astigmatic imaging,[8–11] defocused imaging,[12–18] fluorescence-interference contrast (FLIC) microscopy,[19] focal depth modulation of excitation beam,[20] and intensity decay of an evanescent field.[21] All these techniques are able to achieve a precision of 10–100 nm in localization along the optical axis of the microscope (the *z* dimension) for a single fluorescent object. 3D tracking with confocal imaging and multiple *z*-slice imaging requires relatively complicated and expensive setups and usually trades temporal resolution against imaging volume. The *z* position of objects has been measured by astigmatic and defocused imaging based on the shape and/or orientation of their images. Quantitative dependence on the image shape is a drawback of these two techniques because the recorded intensity distribution of a small fluorescence emitter, the point spread function (PSF), can be markedly perturbed by optical imperfections, such as spherical aberration, polarization, and non-spherical radiative intensity, especially for single dipole emitters.[22, 23] Recently, Yajima et al.[24] developed a 3D tracking technique based on the relative displacement of a pair of split images that are formed by a wedge prism located at the back-focal-plane of the objective. Pavani et al.[25] used the orientation of engineered double-helical PSFs to measure the *z* position of single fluorophores.

*Correspondence should be addressed to Y.E.G (goldmany@mail.med.upenn.edu).

SUPPORTING INFORMATION

Methods and materials, simulation of *Parallax* split views, calibration of *Parallax*, and comparison of the expected localization accuracy of z position using *Parallax* and astigmatic imaging techniques.

In this work, we developed a 3D tracking microscopy system, termed *Parallax*. The method involves only simple modification to the imaging path using commercially available mirrors. *Parallax* allows tracking single fluorescent molecules or other objects in 3D with high localization precision and temporal resolution. As example applications, we use *Parallax* to track the 3D motion of GLUT4-containing vesicles in living adipocytes as they approach the plasma membrane under insulin stimulation and single myosin VI molecules that follow a helical path walking along actin filaments. We also show that *Parallax* is a useful optical 3D profiling tool for larger objects by tracking the profiles of actin filaments in solution away from a surface.

The split images in *Parallax* are generated by a pair of closely spaced, nearly parallel mirrors placed at a plane conjugate to the objective back focal plane (Fig. 1a). A lens (f = 40 mm) is placed one focal length away from the image plane near the side port of the microscope. The beam flux from a small object becomes collimated after the lens and is split into two paths by the mirrors placed one focal length farther away. The sharp edge of the front mirror is positioned so that it reflects half of the beam while the other half passes by to the back mirror. Both beams are then re-guided toward the camera by a third mirror and an image forming focusing lens (f=100 mm). The two images on the camera chip are separated by approximately half of the image height, Δy_1, in the upper and lower halves of the detector area (Figs. 1a and 1b). They correspond to the view of the object by the objective from the two sides of the optical axis, above and below the optical midline in Fig. 1a. Under this optical configuration, when the object moves only in the *xy* plane, both of its images move the same amount in the *x* and *y* directions. When the object moves along the *z* direction, it goes out of focus and its two images move toward or away from each other in the *y* direction. The middle diagram in Fig. 1a illustrates the case when the object moves away from the focal plane. The split beams are focused in front of the camera chip and the projected images formed on the camera move closer to each other (separation Δy_2) than when the object is in focus (separation Δy_1). The difference between Δy_1 and Δy_2 provides the displacement of the object in the *z* direction (Δz), while the in-plane (*x* and *y*) positions of the object are obtained from the average of the two image positions.

As *Parallax* uses half of the objective to form each image, the point spread function (PSF) is no longer a circular Airy disk. Instead, as shown by a simulation (Figs. 1c and S1), the PSF is stretched along the axis that is perpendicular to the split plane and the shape of the in-focus PSF becomes an oval. For out of focus images the shape of the PSF is more complex, gaining a triangular shape.

Fluorescent beads (1:1000 dilution in deionized water. Molecular Probes, FluoSpheres, 0.2 μm, 540/560, 2% solids) immobilized on a glass cover slip were used to calibrate the *Parallax* setup. A nanostage (Mad City Labs) was used to move the bead slide in programmed steps. In Fig. 1b-e, the sample is moved up and down along *z* axis by the nanostage in 40 nm steps giving a total travel distance of 2 μm. The upper and lower halves of the image in Fig. 1b show the pairs of images of the fluorescent beads. The images of beads are stretched along the *y* direction as predicted by the calculated PSFs (Figs. 1c and S1). For the purpose of demonstration, the images of the upper (red dots) and lower panels (green dots) are superimposed using $z = 0$ as the reference frame (Fig. 1c). When the nanostage moves the bead slide from 560 nm below the focal plane to 560 nm above the focal plane, the red and green images move towards each other along *y* axis as expected. A 2D Gaussian function is fitted to the images to locate their centers. The distance Δy between the split images of a bead changes linearly with its *z* position within about ±1 μm relative to the focal plane. In Fig. 1d, the linear fits of data during upward motion (red symbols) and downward motion (blue symbols) return a slope ($\Delta y/\Delta z$) of −0.876.

However, using a nanostage to move a fluorescent bead fixed on a coverslip is not equivalent to the case where the object moves up and down in water because of the mismatch in refractive indices between the glass and water. In order to obtain the effective calibration factor ($\Delta y/\Delta z$) for an object in aqueous solution, we prepared a sample of fluorescent beads trapped in an agarose gel (1.3%) and used the nanostage to track the same group of beads for their depth under a 60X water immersion objective and the 100X oil immersion objective used on the *Parallax* setup. Because the refractive index of a 1.3% agarose gel is about 1.33,[15, 26] close to that of water, a comparison of the depth of the same beads measured in the agarose gel using the water and oil objectives gives the focal shift between the apparent depth with the oil objective and the actual depth. Fig. 1e shows the depth of 22 agarose trapped beads measured with the oil objective vs. that measured with the water objective. The focal shift ratio given by the slope of the linear fit, 1.35, is somewhat greater than the ratio of the refractive indices (1.51/1.33=1.135), as others have also found for similar comparisons.[9, 27] The effective calibration factor ($\Delta y/\Delta z$) for the *Parallax* setup comes out to be −1.17, the product of the apparent calibration factor in Fig. 1d and the focal shift ratio in Fig. 1e. The calibration and focal shift is presumably different for other microscopes. We also noticed that the apparent calibration factor in Fig. 1d is not exactly constant. Instead, it changes linearly with the depth of the object in aqueous solution or with the focal position of the objective at a rate of about 7% per micrometer (Fig. S2). Therefore, the effective calibration factor, −1.17, is only appropriate for objects near the substrate, which is generally true for *in vitro* and *in vivo* assays using total internal reflection fluorescence microscopy (TIRFM). Thus, for 3D tracking deeper in solution, the calibration factor would be slightly altered.

The precision of the bead position tracking is related to the standard deviation, σ_x and σ_y, of the 2D Gaussian fitting of the point spread function and shown in Fig. 1f as a function of the *z* position of the bead. The defocused images distort much more in *x* direction than they do in *y* direction as expected from simulated PSF (Fig. S1). Overall, σ_x and σy are maintained below 200 nm within ±500 nm displacement in the *z* direction. Given a photon number of about 40,000 for a fluorescent bead, the theoretical accuracy of localizing the center of a bead is about 1 nm in the *x* direction, 2 nm in the *y* direction, and 3 nm in the *z* direction ($\sigma_z = \sqrt{2}\sigma_y$, see Ref.28 and Supporting Info. for details).

To check whether there is any crosstalk between the displacement in the *z* and *x*-*y* directions, we stepped the nanostage along the *x* (100 nm/step) and *z* (50 nm/step) directions alternately (Figs. 2 and S3). The level of crosstalk is defined as the ratio of the apparent change of average *x* position and the displacement in the *z* direction by the nanostage, and *vice versa*. The crosstalk is random and small (mostly within ±10%), which may be largely attributed to the axis motion crosstalk of the nanostage and mechanical and thermal drift of the sample. Therefore, *Parallax* tracking in one dimension does not introduce substantial artifacts into measurement of motions in the other dimensions.

We used *Parallax* to track the 3D movement of GLUT4-containing vesicles in living adipocytes. GLUT4 is a major glucose transporter in adipose and muscle tissue localized primarily in an intracellular vesicle storage compartment under basal conditions. Following insulin stimulation, GLUT4-containing vesicles traffic to the cell surface where they fuse with the plasma membrane in an actin and microtubule-dependent manner.[29, 30] We tracked vesicles containing a genetically encoded fluorescent GLUT4 protein construct (GFP-GLUT4) following insulin stimulation. Fig. 3a shows the 3D movement of a GFP-GLUT4-containing vesicle at 100 ms intervals as it enters the TIRF illumination field (left-hand side) and moves ~800 nm in the *x* direction. It then moves ~200 nm closer to the coverslip where its movement is restricted. Fig. 3b shows another vesicle approaches the coverslip and remains there for ~ 6 seconds.

Parallax also enables high precision tracking of single organic fluorophores in 3D. Fig. 4 shows a bifunctional-rhodamine (BR) labeled myosin VI[31] tracked by *Parallax* as it steps along an actin filament. The actin filament is raised off the surface at one end by a microtubule attached to the slide to create an artificial slope and clearance underneath. The displacement of the fluorophore on the myosin VI lever arm along the actin filament clearly shows individual steps of the molecule (Fig. 4a). The actin filament is assumed to be a straight line (orange in Fig. 4b) fit through the 3D trajectory of the myosin VI molecule, given that the persistence length of actin filaments (~17 μm)[32] is much larger than the travel distance (~500 nm). The 3D trajectory of myosin VI in Fig. 4b shows that the myosin VI molecule walks up along the actin filament and follows a right-handed helical path as reported previously.[31]

Besides the 3D positioning of single punctate objects, it is also useful to know the 3D profiles of more complex structures such as cytoskeletal networks. Here we show that *Parallax* is capable of tracking 3D profiles of actin filaments that are suspended over microfabricated features. The dark parallel stripes in Fig. 5a are poly(methyl methacrylate) (PMMA) ridges (height ~ 350 nm, width ~ 1 μm) and grooves (width ~ 2 μm) prepared with soft lithography. The dimension of the micro-fabricated PMMA features were measured using a Vecco Bioscope II atomic force microscope (AFM) (data not shown). Actin filaments that have color contours are fitted with a 2D Gaussian wall function[19] and their 3D profiles (Fig. 5c) are obtained by *Parallax*. The 2D (Fig. 5b) and 3D view (Fig. 5c) both show that actin filaments track the features of the PMMA pattern and sag into the grooves. The red actin filament suspended almost straight across ridges at 5000 and 8000 nm. The dimensions of the profile features of actin filaments suggest that *Parallax* tracks the 3D profiles at reasonable precision. For instance, all vertical peak-to-valley distances of actin filaments are about 350 nm, consistent with the height of the PMMA ridges. The right portion of the red actin filament, which crosses over the groove, is also about 350 nm high. The horizontal peak-to-valley distance of each actin filament is about 1–2 μm, consistent with the half pitch (1.5 μm) of the PMMA features.

Unlike the astigmatism and defocused imaging techniques recently reported for tracking small fluorescent objects, the *Parallax* 3D tracking technique does not rely on the shape or orientation of the image to determine the *z* position of an object. Instead, the displacement in the *z* direction is linearly related to the relative distance in the *y* direction between each pair of spots in the split images, the centers of which can be precisely measured, giving *Parallax* a few advantages over the astigmatic and defocused imaging techniques. Firstly, the localization precision of *Parallax* is quite insensitive to the shape of the PSF thus is not limited by aberrations and polarization. Secondly, methods that depend on the shape of a PSF are inherently less accurate in *z* localization because determination of a shape parameter is statistically less robust than determination of the center. For instance with ideal imaging and equivalent total numbers of collected photons per object, astigmatic depth detection based on the relative *x* to *y* width of the spots[9, 10] is theoretically about 30% less precise than that measured by *Parallax* (see Supporting Info. for details). Thirdly, because astigmatism and defocused 3D tracking techniques are based on the shape of images, they are inherently unable to track the 3D position of any objects, such as actin and microtubules, which are not point emitters or round. On the contrary, using either the centers of point objects or the longitudinal center line of a chain, *Parallax* can resolve the 3D profiles of complex objects as demonstrated in Fig. 5. *Parallax*, by itself, as a diffraction-limited optical imaging method, cannot revolve dense or complicated structures; nor can it track the *z* positions of filaments aligned in the *y* direction as the images are split in the *y* direction. These limitations can be removed by combining *Parallax* with super-resolution imaging methods that resolve point emitters.[33–35]

The 3D imaging method based on split images with a prism, developed by Yajima et al.[24], is similar, in principle, to the *Parallax* 3D imaging described here. However, there are subtle differences in practice. Due to the brevity of description by Yajima et al.,[24] differences in

distortion of the PSF using the different ways to split light, and the optical aberrations produced by the prism cannot be evaluated. The following advantages apply to our method: (1) The positioning of the two mirrors is flexible and easy. They can be positioned at any back focal conjugate plane to accommodate the various optical configurations. (2) The spitting of light is adjustable because both mirrors have freedom in all three dimensions. This feature is useful for positioning the split views at optimal locations on the camera chip. (3) The mirror method, using commercially available components, is cost effective. (4) The edge of a mirror can be made very sharp, thus providing ideal splitting of light, adjustable between the two halves of the objective's catchment. (5) The overall flexibility of the *Parallax* 3D imaging module makes it portable and transferrable onto other optical microscopy setups.

In conclusion, *Parallax* allowed 3D imaging with nm spatial precision of GLUT4-containing vesicles in living adipocytes. Long-range movements of vesicles are consistent with GLUT4 movement along microtubules.[36] Indeed, in cells co-transfected with GFP-GLUT4 and mCherry-human-alpha-tubulin, long-range movements in the *x* direction corresponded with the location of microtubules (data not shown). Movements of GLUT4-containing vesicles in the *z* direction are consistent with the known redistribution of these vesicles from intracellular stores to the plasma membrane in response to insulin. *Parallax* is also capable of tracking single fluorescent myosin VI molecules in 3D. Motor proteins often travel less than 100 nm in the *z* direction relative to their tracks, a range where *Parallax* has high spatial precision. As an extension to the 2D FIONA imaging technique, the *Parallax* technique is very simple to implement, the data analysis is straightforward, and it provides high temporal resolution and precision. It is expected to facilitate 3D super-resolution imaging with switchable fluorophores as described recently in several papers.[33–35]

Supplementary Material

Refer to Web version on PubMed Central for supplementary material.

Acknowledgments

The work was funded by NSF grant NSEC DMR04-25780 and NIH grant GM086352. We acknowledge helpful discussion and comments by John F. Beausang and Dr. Martin Pring. We thank Dr. Mitsuo Ikebe for providing the myosin VI construct and Felix Ruhnow for the Matlab program used to track the profile of actin filaments.

References

1. Dinsmore AD, Weeks ER, Prasad V, Levitt AC, Weitz DA. Appl Optics 2001;40(24):4152–4159.
2. Levi V, Ruan Q, Gratton E. Biophys J 2005;88:2919–2928. [PubMed: 15653748]
3. Török P, Wilson T. Opt Commun 1997;137(1–3):127–135.
4. Bornfleth H, Edelmann P, Zink D, Cremer T, Cremer C. Biophys J 1999;77(5):2871–2886. [PubMed: 10545385]
5. Li D, Xiong J, Qu A, Xu T. Biophys J 2004;87:1991–2001. [PubMed: 15345575]
6. Thomann D, Rines DR, Sorger PK, Danuser G. J Microsc 2002;208:49–64. [PubMed: 12366597]
7. Watanabe TM, Higuchi H. Biophys J 2007;92:4109–4120. [PubMed: 17369416]
8. Holtzer L, Meckel T, Schmidt T. Appl Phys Lett 2007;90:053902–053904.
9. Huang B, Wang W, Bates M, Zhuang X. Science 2008;319:810–813. [PubMed: 18174397]
10. Kao HP, Verkman AS. Biophys J 1994;67:1291–1300. [PubMed: 7811944]
11. Ragan T, Huang H, So P, Gratton E. J Fluoresc 2006;16(3):325–336. [PubMed: 16544202]
12. Juette MF, Gould TJ, Lessard MD, Mlodzianoski MJ, Nagpure BS, Bennett BT, Hess ST, Bewersdorf J. Nat Methods 2008;5(6):527–529. [PubMed: 18469823]
13. Prabhat P, Ram S, Ward ES, Ober RJ. Proc of SPIE 2006;6090:60900L.

14. Ram S, Prabhat P, Chao J, Ward ES, Ober RJ. Biophys J 2008;95(12):6025–6043. [PubMed: 18835896]
15. Speidel M, Jonáš A, Florin EL. Opt Lett 2003;28:69–71. [PubMed: 12656488]
16. Toprak E, Balci H, Blehm BH, Selvin PR. Nano Lett 2007;7(7):2043–2045. [PubMed: 17583964]
17. van Oijen AM, Köhler J, Schmidt J, Müller M, Brakenhoff GJ. Chem Phys Lett 1998;292(1–2):183–187.
18. Zhang Z, Menq CH. Appl Optics 2008;47(13):2361–2370.
19. Nitzsche B, Ruhnow F, Diez S. Nat Nanotech 2008;3:552–556.
20. McHale K, Berglund AJ, Mabuchi H. Nano Lett 2007;7(11):3535–3539. [PubMed: 17949048]
21. Singh-Zocchi M, Dixit S, Ivanov V, Zocchi G. Proc Natl Acad Sci USA 2003;100(13):7605–7610. [PubMed: 12808129]
22. Toprak E, Enderlein J, Syed S, McKinney SA, Petschek RG, Ha T, Goldman YE, Selvin PR. Proc Natl Acad Sci USA 2006;103(17):6495–6499. [PubMed: 16614073]
23. Toprak E, Selvin PR. Annu Rev Biophys Biomol Struct 2007;36:349–369. [PubMed: 17298239]
24. Yajima J, Mizutani K, Nishizaka T. Nat Struct Mol Biol 2008;15(10):1119–1121. [PubMed: 18806799]
25. Pavani SRP, Thompson MA, Biteen JS, Lord SJ, Liu N, Twieg RJ, Piestun R, Moerner WE. Proc Natl Acad Sci USA 2009;106:2995–2999. [PubMed: 19211795]
26. Gibson SF, Lanni F. J Opt Soc Am A 1992;9(1):154–165. [PubMed: 1738047]
27. Egner, A.; Hell, SW. Abberations in Confocal and Multi-Photon Fluorescence Microscopy Induced by Index Mismatch. In: Pawley, JB., editor. Handbook of Biological Confocal Microscopy. Vol. 2. Springer; New York, NY: 1995.
28. Yildiz A, Forkey JN, McKinney SA, Ha T, Goldman YE, Selvin PR. Science 2003;300:2061–2065. [PubMed: 12791999]
29. Zaid H, Antonescu CN, Randhawa VK, Klip A. Biochem J 2008;413:201–215. [PubMed: 18570632]
30. Kanzaki M. Endocr J 2006;53(3):267–293. [PubMed: 16702775]
31. Sun YHWS III, Beausang JF, Homma K, Ikebe M, Goldman YE. Mol Cell 2007;28:954–964. [PubMed: 18158894]
32. Ott A, Magnasco M, Simon A, Libchaber A. Phys Rev E 1993;48:R1642–R1645.
33. Hess ST, Girirajan TPK, Mason MD. Biophys J 2006;91(11):4258–4272. [PubMed: 16980368]
34. Betzig E, Patterson GH, Sougrat R, Lindwasser OW, Olenych S, Bonifacino JS, Davidson MW, Lippincott-Schwartz J, Hess HF. Science 2006;313(5793):1642–1645. [PubMed: 16902090]
35. Bates M, Huang B, Dempsey GT, Zhuang X. Science 2007;317(5848):1749–1753. [PubMed: 17702910]
36. Lizunov VA, Matsumoto H, Zimmerberg J, Cushman SW, Frolov VA. J Cell Biol 2005;169:481–489. [PubMed: 15866888]

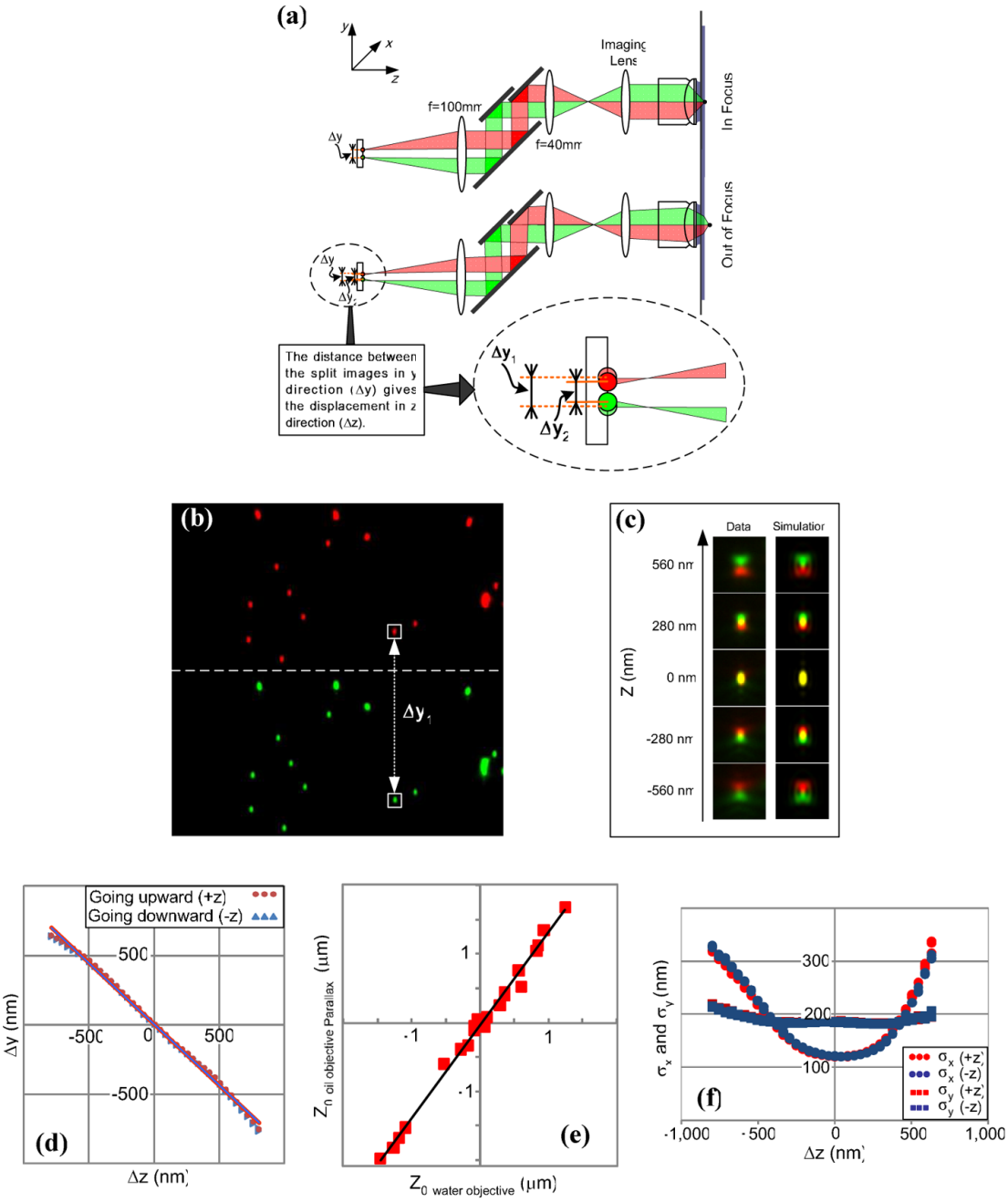

FIGURE 1.

A schematic illustration and characterization of the *Parallax* setup. The red and green colors in (a-c) denote separate portions of the split light paths (a) and resulting pairs of images (b and c). (a) A schematic illustration of the *Parallax* setup. Upper diagram: when a small object is in focus, its beam flux is collimated by a f = 40 mm lens placed one focal length from the primary image plane. With a pair of mirrors placed one focal length farther away, the beam flux is split into two paths that form two images on the upper and lower halves of the camera chip separated by Δy_1. Lower plot: when the object goes out of focus (farther from the objective), its beam flux is no longer collimated and the split images formed on the camera are closer to each other with separation of Δy_2, see the magnified inset. The difference between

Δy_1 and Δy_2 provides the signal for measuring displacement of the object in the *z* direction (Δz); (b) Immobilized 200 nm dia. fluorescent beads imaged with the *Parallax* setup. The upper and lower halves of the image show the paired images; (c) The fluorescent beads were moved up and down along *z* axis by a nanostage. The images of the upper panel (red) and lower panel (green) were superimposed using $z = 0$ as the reference frame to demonstrate how the split images in the *Parallax* view move relative to each other and become distorted and blurry as an object moves along the *z* direction. A simulation is given to compare with the data; (d) Calibration of the *Parallax* setup. Within about ±1 μm relative to the focal plane, the distance Δy between the split images changes linearly with the *z* position of the bead; (e) The calibration of focal shift between a water immersion objective and an oil immersion objective. 22 fluorescent beads trapped in an agarose gel were moved up or down by the nanostage and the *z* positions of the beads as they came into focus are plotted. The slope of the linear fit gives the focal shift ratio between the apparent depth measured with *Parallax* using the oil objective and the actual depth measured by the water objective. All *z* positions are offset from the *z* position of a bead which comes into focus in the middle of the nanostage travel range; (f) Blurring of PSFs. σ_x and σ_y, determined by fitting a 2D Gaussian function to the data, are maintained below 200 nm within ±500 nm of *z*-displacement. $+z$ and $-z$ refer to the direction of travel of the stage. The curves are similar for the two directions indicating no hysteresis.

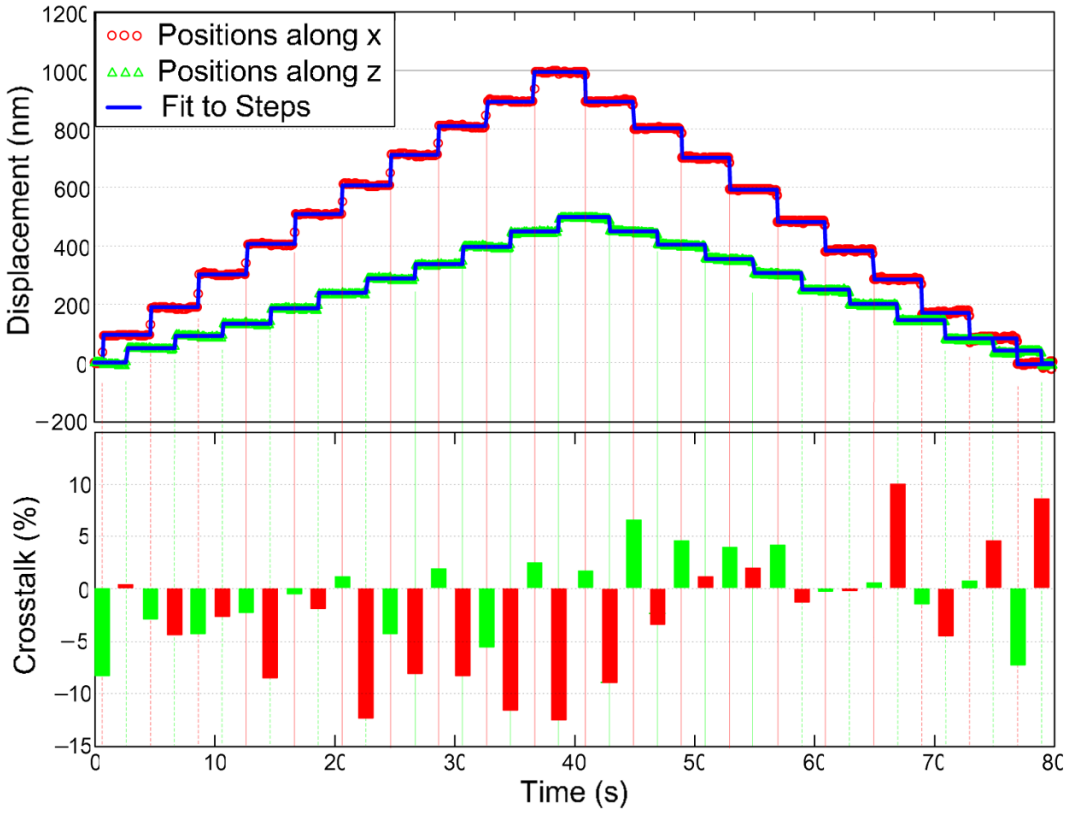

FIGURE 2.

Measurement of the crosstalk between the displacements in the *z* and *x*-*y* directions of the *Parallax* setup. A fluorescent bead sample is moved back and forth by the nanostage along the *x* (100 nm/step) and *z* (50 nm/step) directions alternately. The apparent displacements in the *x* and *z* directions are shown in the upper plot. The definition of crosstalk is given in the text and plotted in the lower plot. Red bars show the change of average *x* position when the sample is moved along the *z* direction, and green bars show the change of average *z* position when the sample is moved along the *x* direction.

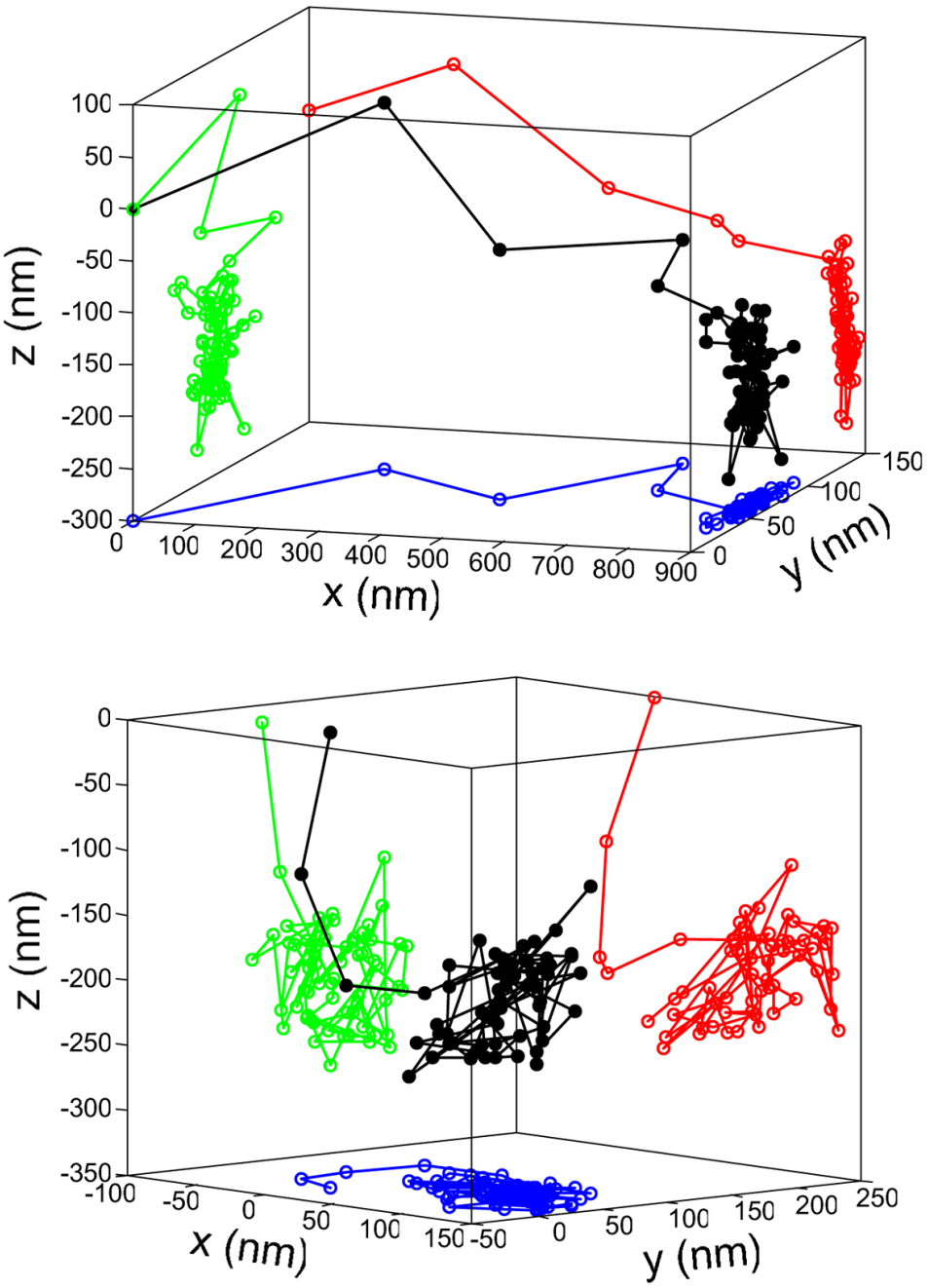

FIGURE 3.

3D tracking of two different GFP-GLUT4-containing vesicles in living 3T3-L1 adipocytes with *Parallax*. Data points were acquired at 100 ms intervals. In both (a) and (b), solid black circles are the 3D trajectory of the GFP-GLUT4 vesicles, and open red, green, and blue circles are the 2D projections of the trajectory onto the *z*-*x*, *y*-*z*, and *x*-*y* planes, respectively.

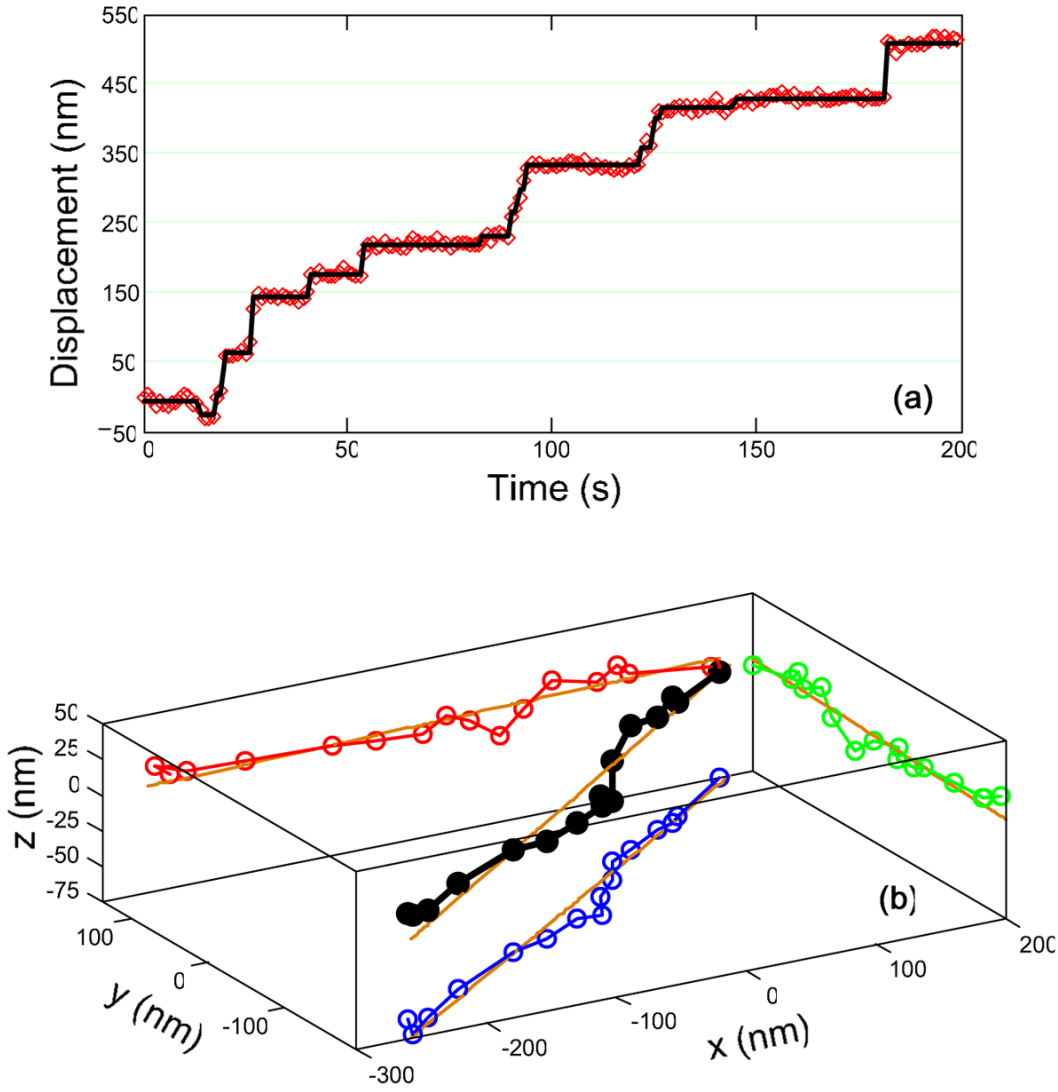

FIGURE 4.

Parallax Tracking bifunctional-rhodamine (BR) labeled myosin VI walking along an actin filament. (a) stepping displacement of myosin VI along the actin filament at 7 μM MgATP; (b) 3D trajectory of the myosin VI molecule. Orange line: actin; Solid black circles: average position of myosin VI during each dwelling period. Open red, green, and blue circles and corresponding orange lines are the 2D projections or the track and trajectory onto the *z*-*x*, *y*-*z*, and *x*-*y* planes, respectively.

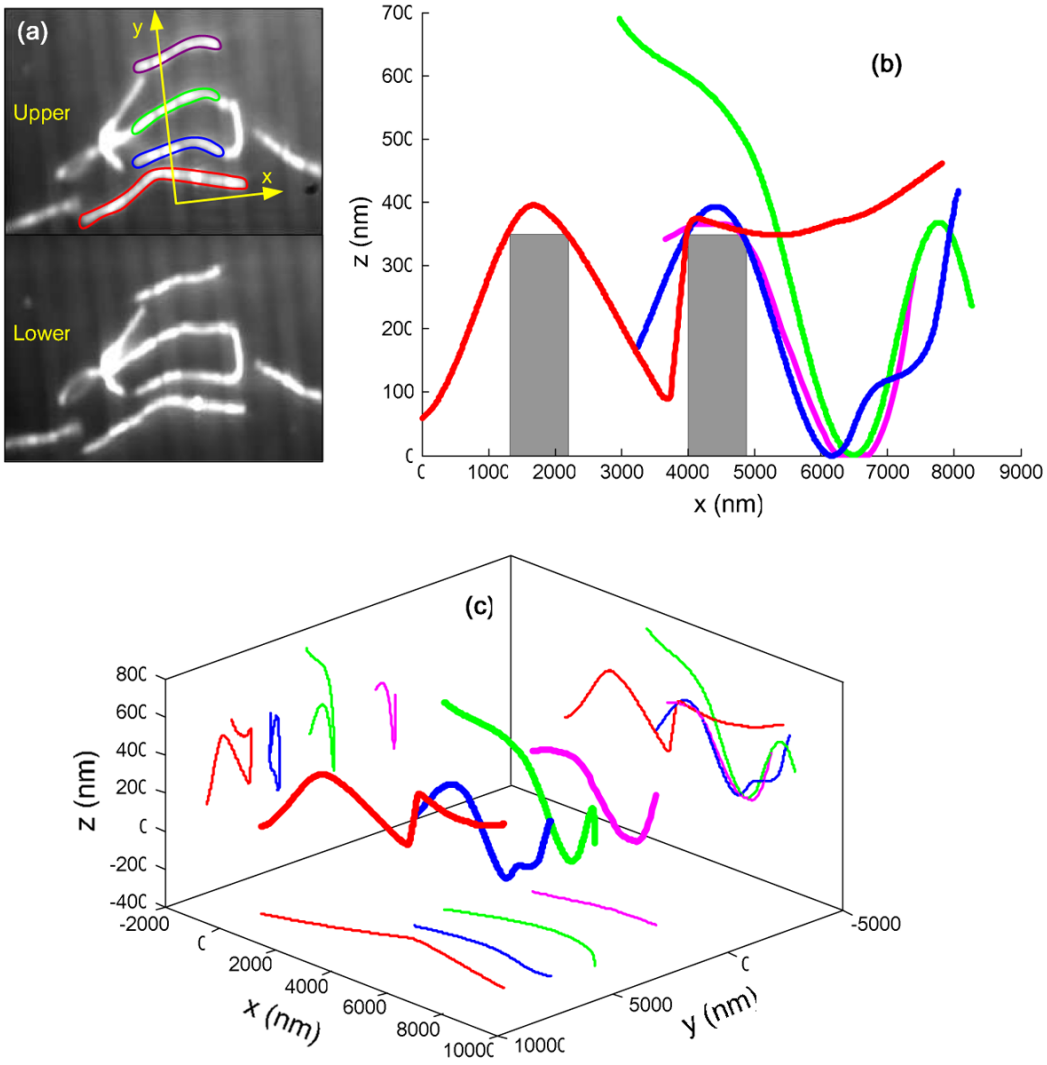

FIGURE 5.

Tracking 3D profiles of actin filaments crossing over surface micro-features with *Parallax*. (a) The upper and lower panels of the *Parallax* view at actin filaments crossing over parallel ridges and grooves prepared by soft lithography. The dark narrower parallel stripes are the ridges about 350 nm tall and 1 μm wide, and the dark wider parallel stripes are the grooves about 2 μm wide. The color contours highlight the actin filaments that are tracked and displayed in (b) & (c). The direction of the ridges is used as the *y* axis in the (b) and (c). (b) 2D view on the *z*-*x* plane shows that most part of the actin filaments sag into the grooves except the right portion of the red actin filament crosses over the groove and hangs on a second ridge. The grey vertical bars stand for the cross section of the ridge. (c) 3D profile and corresponding 2D projections of the actin filaments tracked with *Parallax*.